RSC Advances

PAPER

View Article Online
View Journal | View Issue

Cite this: *RSC Adv.*, 2022, **12**, 9210

Fabrication of a polyoxotungstate/metal–organic framework/phosphorus-doped reduced graphene oxide nanohybrid modified glassy carbon electrode by electrochemical reduction and its electrochemical properties

Hamid Ravanbakhsh, Somayeh Dianat * and Amin Hosseinian

Hybrid nanocomposites based on polyoxometalates (POMs), metal–organic frameworks (MOFs), and graphene oxide (GO) have a unique set of properties. They have specific properties such as high acidity, oxygen-rich surface, and good redox capability from POMs. In contrast, they do not have weaknesses of POMs such as a low surface area, and high solubility in aqueous media. Herein, a novel organic–inorganic nanohybrid compound based on $H_3PW_{12}O_{40}$ (PW_{12}), a Co-based MOF, and GO was prepared. The prepared hybrid nanocomposite (PW_{12}/MOF/GO) was characterized using different techniques. Then, a PW_{12}/MOF/GO nanocomposite modified glassy carbon electrode (GCE) was fabricated by the drop-casting method and next was dried at room temperature. Then, the PW_{12}/MOF/GO/GCE was subjected to electrochemical reduction at a constant potential of −1.5 V, in 0.1 M H_3PO_4 solution containing 0.10% w/v PW_{12}/MOF/GO additive. The morphology, electrochemical activity, and stability of the modified electrode (PW_{12}/MOF/P@ERGO/GCE) were studied with FE-SEM coupled with EDS, CV, and amperometry. The obtained results confirmed that the PW_{12}/MOF/P@ERGO/GCE could be effective in hydrogen evolution reaction (HER). The electrochemical activity of the PW_{12}/MOF/P@ERGO/GCE due to the desirable microstructure of the electrocatalyst (*e.g.* high active surface area and homogeneous distribution of the PW_{12}/MOF/P@ERGO), and also the synergistic effect of the blocks, is more than those of PW_{12}/GCE, MOF/GCE, PW_{12}/MOF/GCE, and P@ERGO/GCE. Moreover, the PW_{12}/MOF/P@ERGO/GCE showed an excellent long-term stability under the air atmosphere.

Received 4th February 2022
Accepted 18th March 2022

DOI: 10.1039/d2ra00746k

rsc.li/rsc-advances

1. Introduction

Polyoxometalates (POMs) are a large class of metal oxide clusters, consisting of early transition metal oxoanions with shared oxygen atoms exhibiting well-defined connectivity.[1,2] POMs, especially Keggin-type POMs, have wide applications in various fields such as catalysis,[3] optics,[4] magnetism,[5] medicine,[6,7] environmental science,[8] and electrochemistry,[9,10] due to their exclusive molecular structure, electronic features, and excellent redox properties. One of the attractive properties of POMs is that the anionic cluster can undergo a fast, stepwise, reversible, and multi-electron transfer reaction while keeping the structural integrity.[11,12] These numerous redox properties make them potential candidates for surface modification, and electrocatalytic studies. However, their use as catalysts is one of the interesting fields for researchers, because of their high acidity, oxygen-rich surface, and redox capability. Despite these special characteristics, POMs still show some weaknesses for their use as a catalyst. First, POMs have a low specific surface area (<10 $m^2\ g^{-1}$), which consequently reduces the availability of reactants, and secondly, their high solubility in aqueous solutions results in low recyclability.[2]

To overcome these challenges and improve electrochemical properties and electrocatalytic performances, immobilization or dispersion of POMs onto porous materials has been proposed.

In the last few decades, many porous solids have been investigated as immobilizers for POMs, like silica, conducting polymers, ion-exchange resin, and carbon materials.[13–16] Since discovering metal–organic frameworks (MOFs), these porous materials have been widely used as potential supports for POMs.[3,17,18]

MOFs are inorganic–organic hybrid crystalline materials are fabricated from metal-containing nodes and organic linkers through coordination bonds. These materials have attracted considerable attention in recent years due to their large surface areas, adjustable pore size, and designable functionalities.

MOFs have shown great potential in gas storage and separation,[19] catalysis,[20–22] sensing,[23,24] drug delivery,[25,26] proton

Department of Chemistry, Faculty of Sciences, University of Hormozgan, Bandar Abbas, 79161-93145, Iran. E-mail: s.dianat@hormozgan.ac.ir; Tel: +98 76 33670121

conduction,[27,28] solar cells,[29,30] supercapacitors[31,32] and biomedicine.[33,34] In addition, MOFs are as a suitable platform for the introduction of guest molecules due to the high accessibility of their internal surface area and regular long-range channels. To date, several active sites have been successfully embedded in the cages of MOFs, such as noble metals,[35] metal oxides,[36,37] enzymes,[38,39] and POMs.[40,41]

The first report of a POM/MOF hybrid was presented in 2005 by Férey *et al.*[42] In this study, $K_7PW_{11}O_{39}\cdot nH_2O$ successfully was incorporated into big cages of the highly stable Cr-based MOF, MIL-101, using the impregnation method.

Up to now, several other thermal and stable chemical MOFs such as Materials of Institute Lavoisier Framework Series (MIL Series),[43,44] Zeolite Imidazole Framework Series (ZIF Series),[45] and Cu-BTC[46,47] frameworks applied as supports for POMs hosting for using in catalysis.

The most examined POMs that have been incorporated into MOFs are the well-known Keggin $[XM_{12}O_{40}]^{n-}$ and Wells–Dawson $[X_2M_{18}O_{62}]^{n-}$ (X = Si, P, *etc.*; M = Mo, W, V, *etc.*) POMs and their derivatives.[40,48–51]

There are many benefits to using MOFs as a host matrix to encapsulate POMs. First, their extremely high surface areas and confined cages/channels allow the homogeneous distribution of POM in the MOF host to be ensured. This phenomenon prevents the a aggregation of POMs, and improves their stability and recyclability. Secondly, the very regular cages and channels of MOFs provide a high substrate selectivity, or, in other words, only specific substrates/products can access the active POM sites. Thirdly, due to the excellent interaction and electron transfer between the MOF and the POM, an enhanced synergistic catalytic effect is typically observed. Finally, the POM@MOF hybrids not only combine the exciting properties of POM and MOF, but also allow the weaknesses as mentioned above of POMs to be resolved, and the catalytic performance significantly increased.[2]

On the other hand, immobilization or entrapment of POMs on various supporting carbon materials has concerned significant attention. Among the carbon materials, graphene extensively studied in nanotechnology fields due to its excellent chemical stability, high surface area, extraordinary conductivity, and good mechanical properties.[10,12]

Graphene was discovered at Manchester University by Andre Geim and Kostya Novoselov in 2004.[52] It is an allotrope of carbon-containing a single layer of atoms arranged in a two-dimensional (2D) hexagonal lattice nanostructure.[53]

It is the thinnest and most robust known material in the universe.[54] Graphene is a good choice for POMs support materials to overcome the limitations of POMs such as high solubility in polar solvents and low specific surface area (SSA).[55] In addition, the unique features of POMs, especially in catalysis,[56] electrocatalysis,[57] and capacitance,[58] enhance because of the large SSA and excellent electrical conductivity of graphene.

Recently, numerous reports have submitted on the nanocomposites of reduced graphene oxide (RGO) and polyoxometalates (POMs).[58–61] However, the RGO is processed from GO through UV-photoreduction,[62,63] and chemical reduction with hazardous materials.[64] However, using these approaches, POM/RGO composites are obtained in powder form, which must be deposited on the surface of electrode by the drop-casting technique. The drop-casting technique has inherent defects like lack of control over the film thickness and low stability.[65] The self-assembly method is the best way to create stable and uniform modified surfaces. Recently, the preparation of RGO from GO by the electrochemical reduction method has attracted a lot of attention due to its easy and green preparation method.[65–68] Chen *et al.* directly deposited RGO onto a glassy carbon electrode (GCE) through cyclic voltammetric (CV) reduction of a GO colloidal solution. The graphene-modified electrode was applied to simultaneously determine of hydroquinone and catechol.[66] Guo *et al.* investigated the preparation

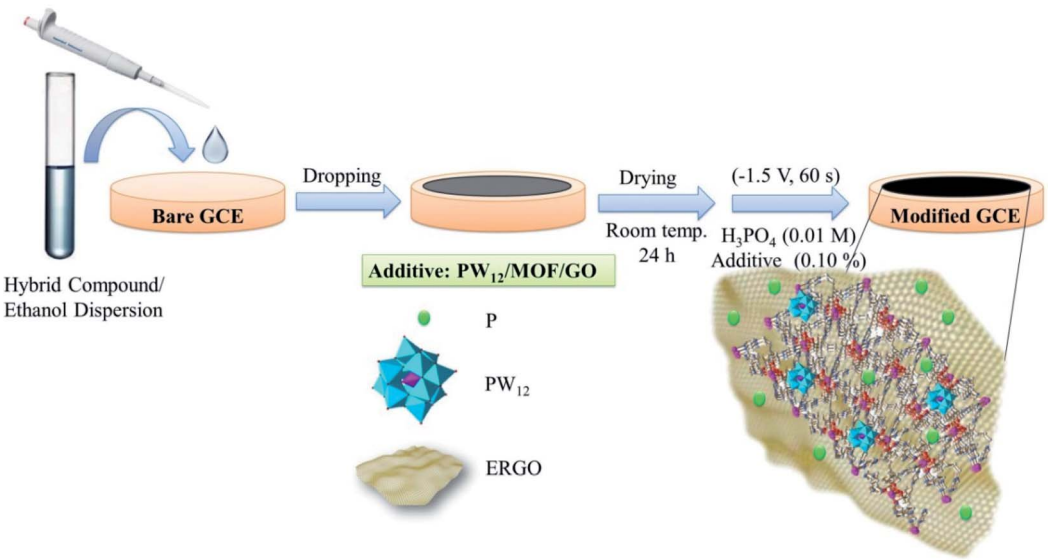

Scheme 1 Schematic diagram of stepwise electrode modification processes.

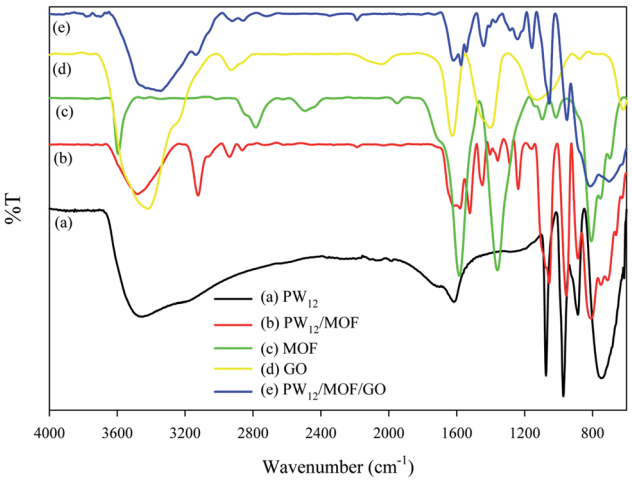

Fig. 1 ATR-FTIR spectra of PW_{12} (a), PW_{12}/MOF (b), MOF (c), GO (d), and PW_{12}/MOF/GO (e).

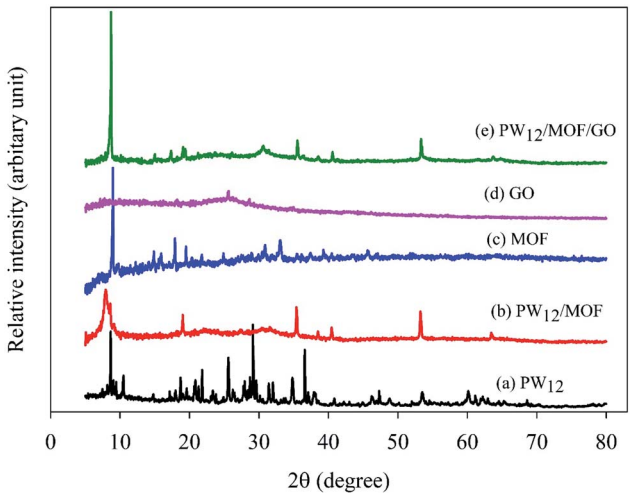

Fig. 2 XRD patterns of (a) PW_{12}, (b) PW_{12}/MOF, (c) MOF, (d) GO, and (e) PW_{12}/MOF/GO.

method and electrocatalytic property of $H_4SiMo_{12}O_{40}$ and chitosan/ERGO multilayer composite films on indium tin oxide (ITO) electrode by electrochemical growth method.[65] Tao Wei *et al.* firstly synthesized $H_5PMo_{10}V_2O_{40}$/BTC/RGO nanocomposites for lithium-ion batteries (LIBs) by a facile one-pot method.[69] Wen Zhang and co-workers prepared a POM/MOF/RGO hybrid material *via* a facile hydrothermal process. The prepared hybrid material is used to detect dopamine (DA). The POM/MOF/RGO/GCE presented an excellent catalytic activity toward oxidation of DA owing to matching functionality and structure between the POM, MOF, and RGO.[70]

Recently, many reports have verified that heteroatom doping into graphene (*e.g.*, B, N, P, and S) can increase the electrical conductivity and electrocatalytic activity of RGO in supercapacitor electrodes,[71,72] lithium-ion batteries (LIBs),[73,74] fuel cells,[75,76] and dye-sensitized solar cells.[77]

The preparation of the P-doped graphene monolayer film modified electrode by the electrochemical reduction approach has many benefits. But, few studies have reported concerning the POM/P@ERGO modified electrode and its derivatives. Therefore fabrication of these modified electrodes still have challenges.

In this work, a new $PW_{12}O_{40}\cdot nH_2O$/$[Co(TPA)(bimb)(H_2O)_2]_n$/GO nanocomposite has been deposited onto a GCE using drop-casting method followed by an electrochemical reduction process (PW_{12}/MOF/P@ERGO). For this purpose, PW_{12}/MOF/GO nanocomposite was dropped onto the GCE. Then the modification procedure completed through the electrochemical reduction of GO to RGO at a constant potential of −1.5 V, for 60 s in a H_3PO_4 aqueous solution (0.1 M) containing PW_{12}/MOF/GO (0.10% w/v) as an additive. The PW_{12}/MOF nanocomposite can interact with P@ERGO *via* $P^{\delta+}$ and π-electrons of MOF without any impact on the electronic structure of PW_{12} Keggin type. The synergistic effects of these four-blocks, and specific microstructure of PW_{12}/MOF/P@ERGO nanocomposite provide enhanced electrochemical activity of the modified electrode. Then, electrochemical behavior, stability, repeatability, reproducibility of the modified electrode were investigated, comprehensively.

2. Experimental section

2.1. Materials

The $[Co(TPA)(bimb)(H_2O)_2]_n$ as a Co-based MOF was synthesized according to the previous literature.[78] The 1,4-bis(imidazole)butane (abbreviated as bimb) was prepared according to the previous literature.[79] Tungstophosphoric acid ($H_3PW_{12}O_{40}$, abbreviated as PW_{12}), cobalt(II) nitrate hexahydrate ($Co(NO_3)_2\cdot 6H_2O$), terephthalic acid (abbreviated as TPA), dimethylformamide (abbreviated as DMF), graphite powder (<20 μm), and other chemicals were of analytical grade and

Table 1 FT-IR data ($\bar{\upsilon}$/cm^{-1}) of PW_{12}, PW_{12}/MOF, MOF, GO, and PW_{12}/MOF/GO[a]

Compound	$\bar{\upsilon}$ (C=C)	$\bar{\upsilon}$ (COO^-)	$\bar{\upsilon}$ (C–O)	$\bar{\upsilon}$ (P–O_a)	$\bar{\upsilon}$ (W–O_d)	$\bar{\upsilon}$ (W–O_b–W)	$\bar{\upsilon}$ (W–O_c–W)
PW_{12}	—	—	—	1074	968	887	753
PW_{12}/MOF	1627, 1485	1585	—	1056	953	886	802
MOF	1585, 1360	—	—	—	—	—	—
GO	1627, 1402	1574	1137	—	—	—	—
PW_{12}/MOF/GO	1625, 1445		1164	1060	952	882	819

[a] O_a central oxygen. O_b, O_c bridging oxygen. O_d terminal oxygen.

purchased from commercial sources (Merck or Sigma) and used without further purification. Phosphate buffer saline solutions (PBS, 0.11 M) were prepared by mixing the stock solutions of 0.10 M KCl and 0.01 M H_3PO_4 and then adjusting the pH with 0.5 M NaOH aqueous solution.

2.2. Physical methods

The percent of immobilized PW_{12} on the GO was determined from inductively coupled plasma-optical emission spectrometry (Optima 7300 V ICP-OES spectrometer Brochure-PerkinElmer) by measuring of tungsten contents in the PW_{12}/MOF/GO. FTIR spectra in ATR mode were recorded using a Spectrum Two FT-IR spectrometer (PerkinElmer) in the 4000–600 cm^{-1} range. The crystalline structure of the PW_{12}, $[Co(TPA)(bimb)(H_2O)_2]_n$, PW_{12}/MOF, GO, and PW_{12}/MOF/GO was confirmed using an X-ray diffraction (XRD, PANalytical X'PERT-PRO X-ray diffractometer equipped with Cu Kα radiation, $\lambda = 0.1541$ nm). The morphologies of the PW_{12}/MOF/GO, and GO were studied by transmission electron microscope (TEM, EM10C-100 kV series, Zeiss Co., Germany). The surface morphology and elemental analysis of the bare GCE, P@ERGO/GCE, and PW_{12}/MOF/P@RGO/GCE were determined using

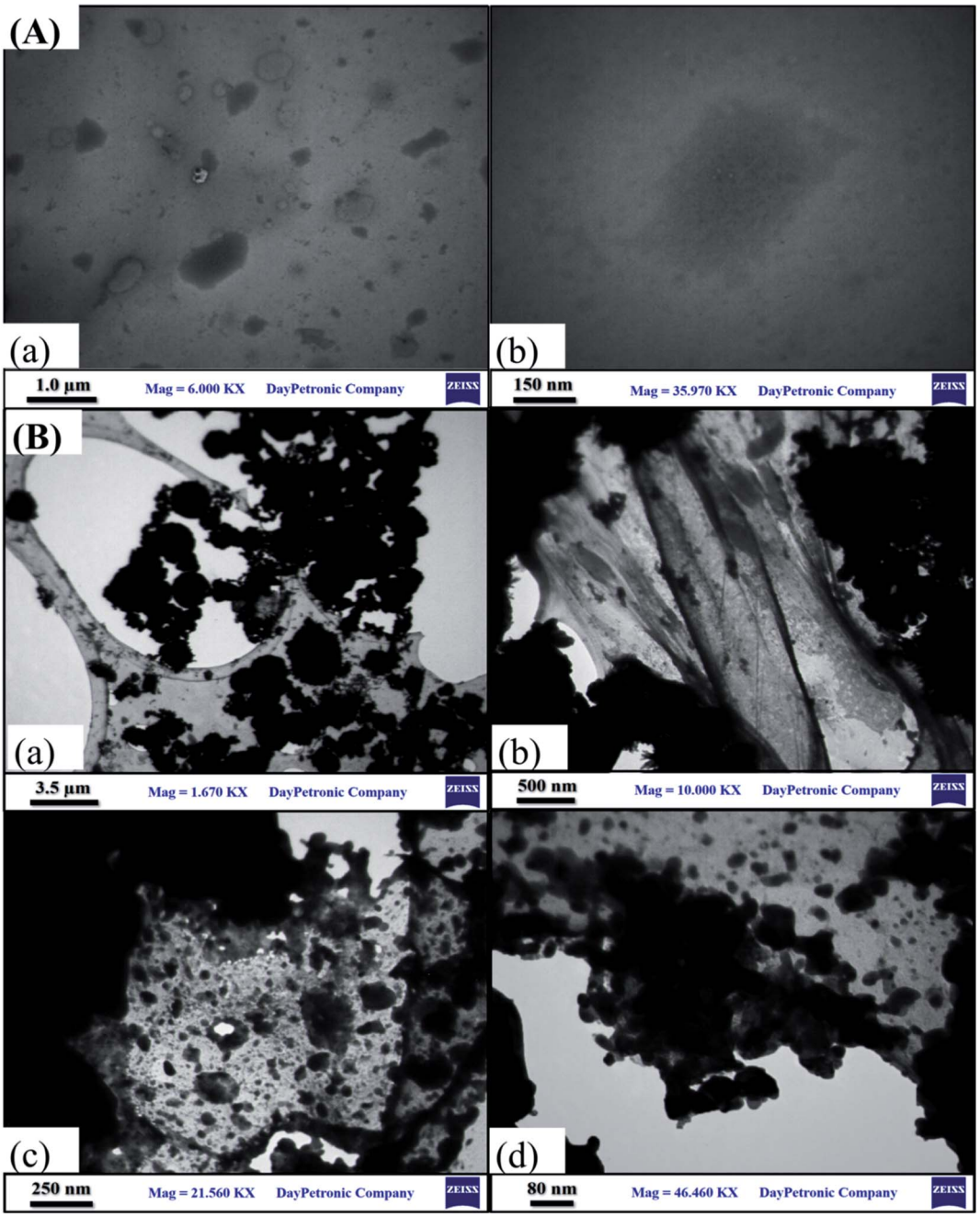

Fig. 3 TEM images of (A) GO (a, b) and (B) PW_{12}/MOF/GO (a–d) at different magnifications.

a Field Emission-Scanning Electron Microscopy (FE-SEM, SIGMA VP, Zeiss Co., Germany), Energy-Dispersive X-ray Spectrometry (EDS) and EDS-mapping. N_2 adsorption–desorption isotherms were recorded at 77 K using a BElSORP Mini-Microtrac Bel Corp instrument. Specific surface areas of MOF and POM/MOF were measured using the Brunauer–Emmett–Teller (BET) method. The pore-size distribution curves were recorded from the isotherm using the Barrett–Joyner–Halenda (BJH) algorithm.

2.3. Electrochemical experiments

The electrochemical experiments were performed with a Metrohm Autolab potentiostat P/GSTAT 302N supplied by Eco-Chemie (Utrecht, The Netherlands). The traditional three-electrode system was used with, an Ag/AgCl (3 M KCl) electrode as the reference electrode, a Pt wire electrode as the auxiliary electrode, and a bare or modified GCE (diameter 2 mm) as the working electrode. Before the electrochemical experiments, Ar gas with the purity of 99.999% was fed into the electrolytic cell for 15 minute. The electrochemical measurements were carried out under the Ar atmosphere at room temperature.

2.4. Synthesis of PW_{12}/MOF

A mixture of bimb (0.095 g, 0.5 mmol), $Co(NO_3)_2 \cdot 6H_2O$ (0.320 g, 1.0 mmol), TPA (0.085 g, 0.5 mmol), and PW_{12} (0.288 g, 1.0 mmol) was dissolved in 25.0 mL DMF and 25.0 mL distilled water. After stirring for 30 minute at room temperature, the reaction suspension was transferred to the Teflon-lined stainless-steel autoclave (100 mL), kept at 160 °C under autogenous pressure for 72 h. Then the autoclave was cooled to room temperature with rate of 5 °C h^{-1}. Reddish-pink crystals were collected by filtration. Then obtained crystals washed with distilled water, and dried in the open air (about 45% yield based on cobalt).

2.5. Synthesis of PW_{12}/MOF/GO

GO was prepared by oxidizing graphite flakes *via* modified Hummers' method.[80] As-prepared GO (0.100 g) in distilled water (10 mL) was exposed to sonication for 30 minute to achieve a homogeneous suspension. Then 1.000 g of PW_{12}/MOF was added. After the sonication for 20 minute, the mixture was transferred into a 100 mL Teflon-lined stainless-steel autoclave. The autoclave was heated in an oven at 180 °C for 24 h. The black precipitates were filtered, washed with distilled water, and dried at 60 °C for 12 h to obtain PW_{12}/MOF/GO.

2.6. Fabrication of PW_{12}/MOF/P@ERGO/GCE

The surface of the GCE was polished with α-alumina slurries (α-Al_2O_3, the particle size of 0.30, 0.10, and 0.05 μm) to remove the contaminants. Then it was electrochemically cleaned in 0.5 M H_2SO_4 solution by repetitive cycling in the potential range from −1.0 to 1.0 V (*vs.* Ag/AgCl) until a stable CV scan is achieved. After rinsing with deionized water, and drying at room temperature, 5.0 μL of the PW_{12}/MOF/GO suspension (0.010 g in 2.0 mL ethanol) was drop-casted onto the bare GCE. Finally, the electrode surface was dried under room temperature overnight at air atmosphere, and washed with deionized water. Then, electrochemical reduction of GO to RGO was performed in 0.01 M H_3PO_4 containing different concentrations of PW_{12}/MOF/GO as additive (0.0, 0.01, 0.05, 0.10, 0.15, and 0.20% w/v) using chronoamperometry in the potential of −1.5 V at various times (30, 45, 60, and 120 s). A better analytical signal was found in the presence of 0.10% w/v PW_{12}/MOF/GO and at time 60 s. Therefore, 0.10% w/v additive and time 60 s were selected as optimum conditions in the fabrication of the modified GCE. PW_{12}/GCE, MOF/GCE, PW_{12}/MOF/GCE, and P@ERGO/GCE, as the control electrodes were constructed by a similar technique in 0.01 M H_3PO_4 in the absence of the additive. The schematic design of the preparation procedure of the modified GCE is displayed in Scheme 1.

2.7. Electrochemical experiment

The electrochemical experiments were done in an electrochemical cell with a volume of 90 mL, containing 5 mL of H_2SO_4 (0.5 M, pH 0.5) solution. The CV, and amperometry methods were used to investigate of electrochemical behavior, effective

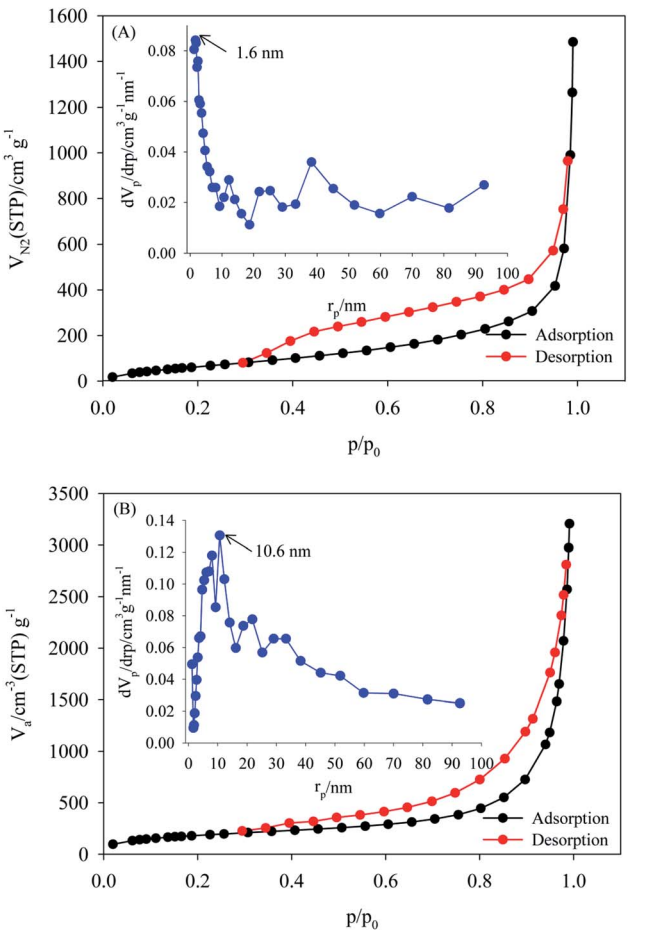

Fig. 4 Nitrogen adsorption–desorption BET isotherms of (A) MOF, (B) PW_{12}/MOF. The insets show the BJH-adsorption pore size distributions.

electroactive surface area, and stability of the modified electrode.

3. Results and discussion

3.1. Characterization

The loading percentage of PW_{12} on GO was estimated 0.83% by ICP spectroscopy. ATR-FTIR spectrum of PW_{12}/MOF/GO is shown in Fig. 1. To prove of structure, ATR-FTIR measurements of PW_{12}, PW_{12}/MOF, MOF, and GO were also recorded as shown in Fig. 1, curves a, b, c, and d, respectively. The information is summarized in Table 1.

The ATR-FTIR spectra of PW_{12}, PW_{12}/MOF, and PW_{12}/MOF/GO show four characteristic peaks, that are related to the stretching vibration of P–O_a, W–$O_{b,c}$–W, and W–O_d. The presence of these asymmetric stretching vibration peaks in PW_{12}/MOF, and PW_{12}/MOF/GO propose that the POM moiety of the hybrid compounds has maintained its Keggin structure. Moreover, the peaks around 1625, 1445, 1574, and 1164 cm^{-1} in PW_{12}/MOF/GO that is assigned to the stretching vibrations of C=C aromatic, COO^-, and C–O confirm the existence of MOF, and GO (compare curve e with c, and d).

The XRD patterns of PW_{12}, PW_{12}/MOF, MOF, GO, and PW_{12}/MOF/GO are presented in Fig. 2. As displayed in Fig. 2b, PW_{12}/MOF shows peaks about 8.2°, and 19.1°, 30.8°, 35.4°, 40.4°, and 53.2°, respectively of the PW_{12} (Fig. 2a). However, a sharp peak about at 8.2°, and a broad peak at 30.8°, which are overlapped with the peaks of PW_{12}, can be credited to the Co-based MOF (Fig. 2c). Fig. 2d shows a broad diffraction peak 26.4°, which is correspond to the (002) plane of GO nanosheets.[81,82] In Fig. 2e, the characteristic XRD peaks of PW_{12}/MOF/GO appeared at nearly similar locations without a significant shift in its peaks position compared to those of PW_{12}, and MOF. However, the peak (002) of GO was not appeared because of peak overlap with the peak of PW_{12}, and MOF which has a higher crystallinity.

The TEM images of the GO and PW_{12}/MOF/GO at the various magnifications are displayed in Fig. 3. TEM images of PW_{12}/MOF/GO show that PW_{12}/MOF nanospheres was immobilized homogeneously on the GO surface. Such homogeneous distribution of the PW_{12}/MOF nanospheres on the surface of GO enhanced the electrochemical activity.

The specific surface areas and pore size distributions of the MOF, and PW_{12}/MOF were measured by N_2 adsorption–desorption isotherms. As shown in Fig. 4A and B, both samples exhibited a type-IV isotherm curve with an H4 hysteresis loop, often associated with narrow slit-like pores. The BET surface areas, total pore volumes, and mean pore diameters for MOF, and PW_{12}/MOF are 277 m^2 g^{-1}, and 697 m^2 g^{-1}, 0.22 cm^3 g^{-1}, and 0.47 cm^3 g^{-1}, 32 nm, and 27 nm, respectively. The pore size distributions were calculated from the adsorption isotherms using the BJH model as shown in the inset of Fig. 4A and B. These confirm that the MOF, and PW_{12}/MOF mainly contain micropores (1.6 nm), and mesopores (10.6 nm), respectively.

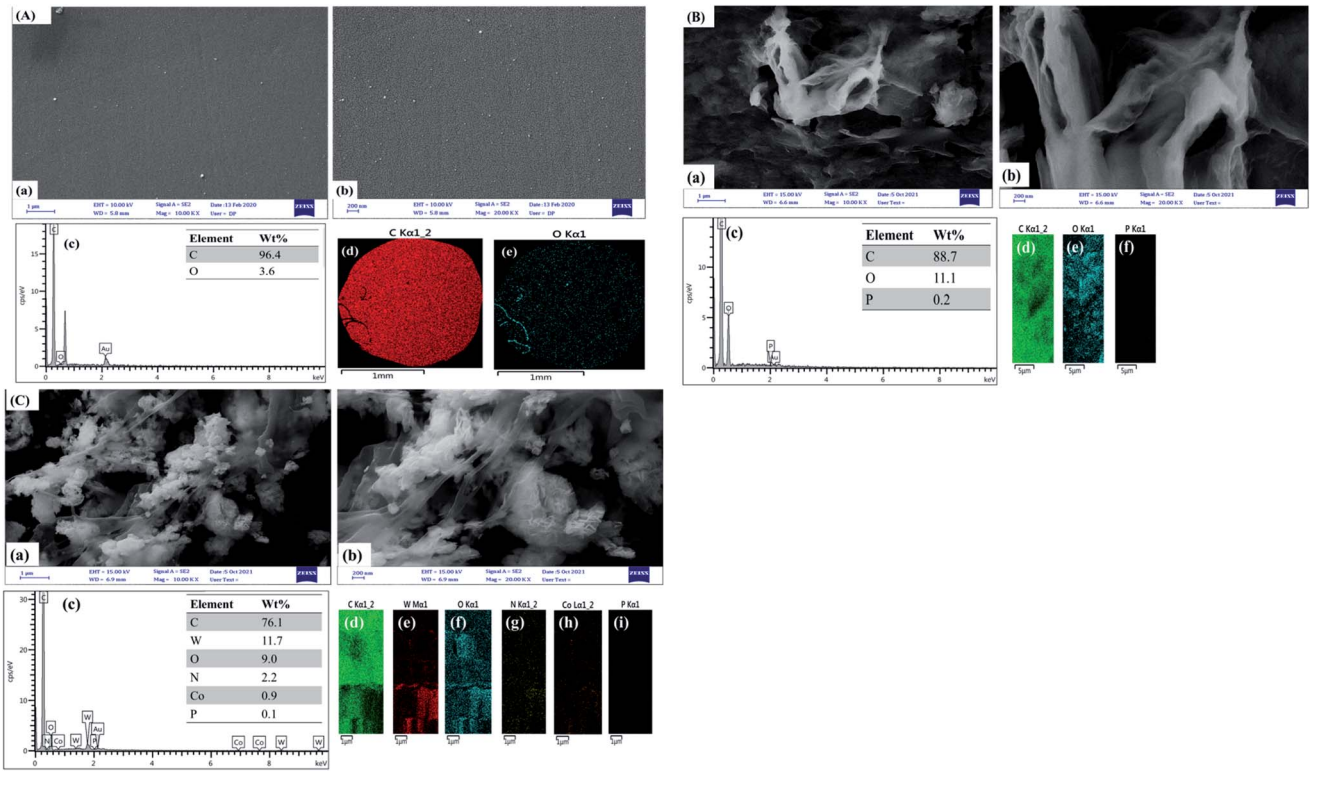

Fig. 5 (A) FE-SEM images (a, b), EDS pattern (c) and EDS element mapping (d, e) of the bare GCE, (B) FE-SEM images (a, b), EDS pattern (c) and EDS element mapping (d–f) of P@ERGO/GCE, and (C) FE-SEM images (a, b), EDS pattern (c) and EDS element mapping (d-i) of PW_{12}/MOF/P@ERGO/GCE.

The morphology of the PW_{12}/MOF/P@ERGO/GCE was characterized using FE-SEM, and compared with bare GCE, and P@ERGO/GCE. The FE-SEM images confirmed that the bare GCE (Fig. 5A, images a, b) have a mirror-like surface, which was changed to roughly and heterogeneously surface after the modification by P@ERGO, and PW_{12}/MOF/P@ERGO (Fig. 5B and C, images a, b). Additionally, the EDS patterns of the bare and modified GCEs are presented in Fig. 5A–C image c. The EDS spectra and elemental mappings approve the presence of C, and O in the bare GCE (Fig. 5A, images c–e), C, O, and P in the P@ERGO/GCE (Fig. 5B, images c–f) and C, W, O, N, Co, and P elements on the PW_{12}/MOF/P@ERGO/GCE (Fig. 5C, images c–i).

3.2. Electrochemical activity of PW_{12}/MOF/P@ERGO/GCE

The electrochemical behaviors of the bare GCE, MOF/GCE, PW_{12}/GCE, PW_{12}/MOF/GCE, P@ERGO/GCE, and PW_{12}/MOF/P@ERGO/GCE were investigated using the CV method in 0.5 M H_2SO_4 (Fig. 6). As shown in curve a, the bare GCE did not show any significant peak. In contrast, MOF/GCE, PW_{12}/GCE, PW_{12}/MOF/GCE, P@ERGO/GCE, and PW_{12}/MOF/P@ERGO/GCE displayed a cathodic peak (peak I) about at −0.2 V (*vs.* Ag/AgCl), that can correspond to hydrogen evolution reaction (HER). However, the peak I current in PW_{12}/MOF/P@ERGO/GCE (curve f) is more significant than MOF/GCE (curve b), PW_{12}/GCE (curve c), PW_{12}/MOF/GCE (curve d), and P@ERGO/GCE (curve e). This result confirms a synergistic effect of four blocks that can promote the electron transfer more effectively.

3.2.1. Effect of scan rate. The CVs of the PW_{12}/MOF/P@ERGO/GCE in H_2SO_4 (0.5 M) at different scan rates were presented in Fig. 6B. As shown in the inset of Fig. 6B, the peak I current depends linearly on the square root of scan rate from 10 to 400 mV s^{-1}. The results show that the HER at the modified electrode undergoes a diffusion-controlled process.

3.2.2. Effect of pH. In Fig. 6C, the impact of buffer pH on the electrochemical activity of the PW_{12}/MOF/P@ERGO/GCE was examined at different pH values (pH 0.5–8.0), using the CV method. As shown in Fig. 6C, peak I, which corresponds to HER, is only seen at pH 0.5 (curve a). This phenomenon can be due to the stability of POMs-based modified electrodes[9,10] and also the performance of HER at acidic pH.[83,84] Therefore, pH 0.5 was considered the optimal pH, and further studies were performed at this pH.

3.3. Optimization of coating parameters

Optimizing of coating parameters is essential to achieve a modified electrode with enhanced electrochemical behavior. Some important parameters, including type, and concentration of electrolyte additive, and deposition time, were investigated. These parameters can affect the electrochemical property of the

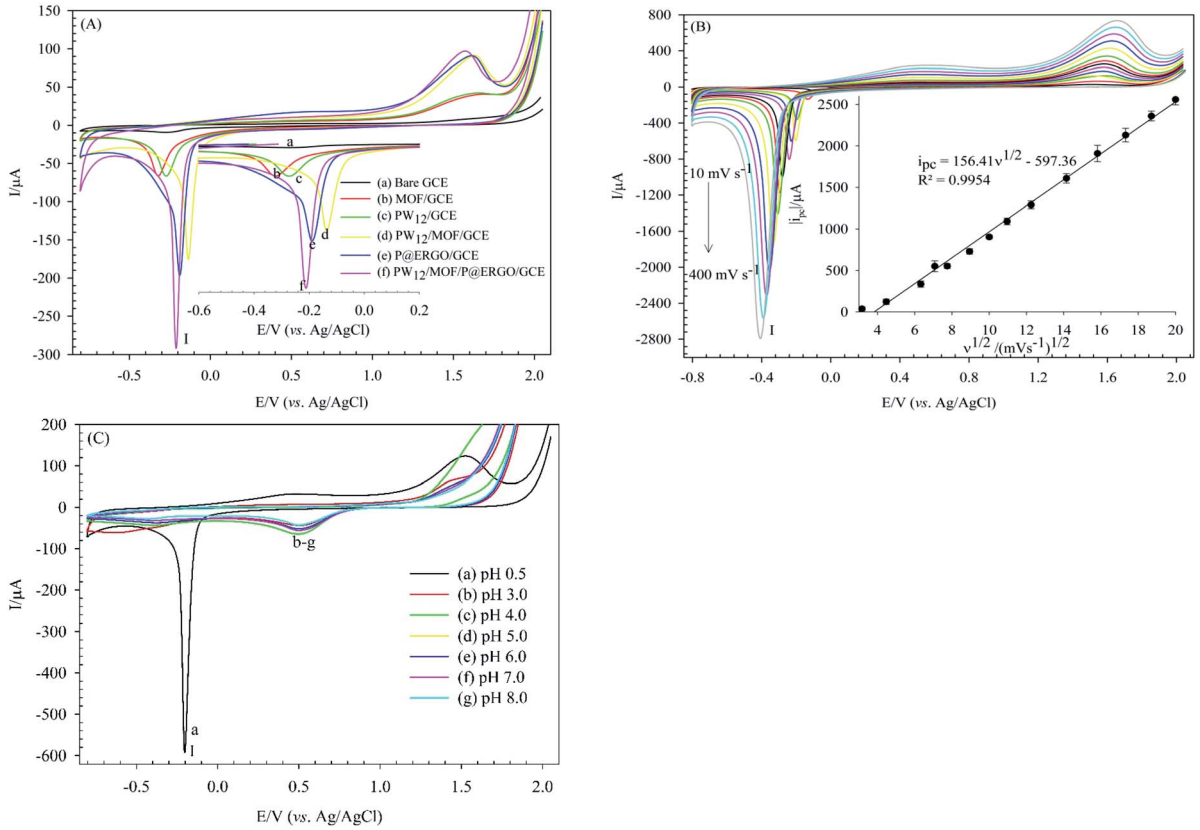

Fig. 6 (A) CVs obtained on the bare GCE (a), MOF/GCE (b), PW_{12}/GCE (c), PW_{12}/MOF/GCE (d), P@ERGO/GCE (e), and PW_{12}/MOF/P@ERGO/GCE (f) in H_2SO_4 (0.5 M, pH 0.5) and scan rate of 50 mV s^{-1}, (B) CVs of the PW_{12}/MOF/P@ERGO/GCE in H_2SO_4 (0.5 M, pH 0.5) at different scan rates from 10 to 400 mV s^{-1}. The inset shows variations of the absolute value of peak I currents with square root of scan rates, and (C) CVs of the PW_{12}/MOF/P@ERGO/GCE at different pHs from pH 0.5 to pH 8.0; scan rate 50 mV s^{-1}.

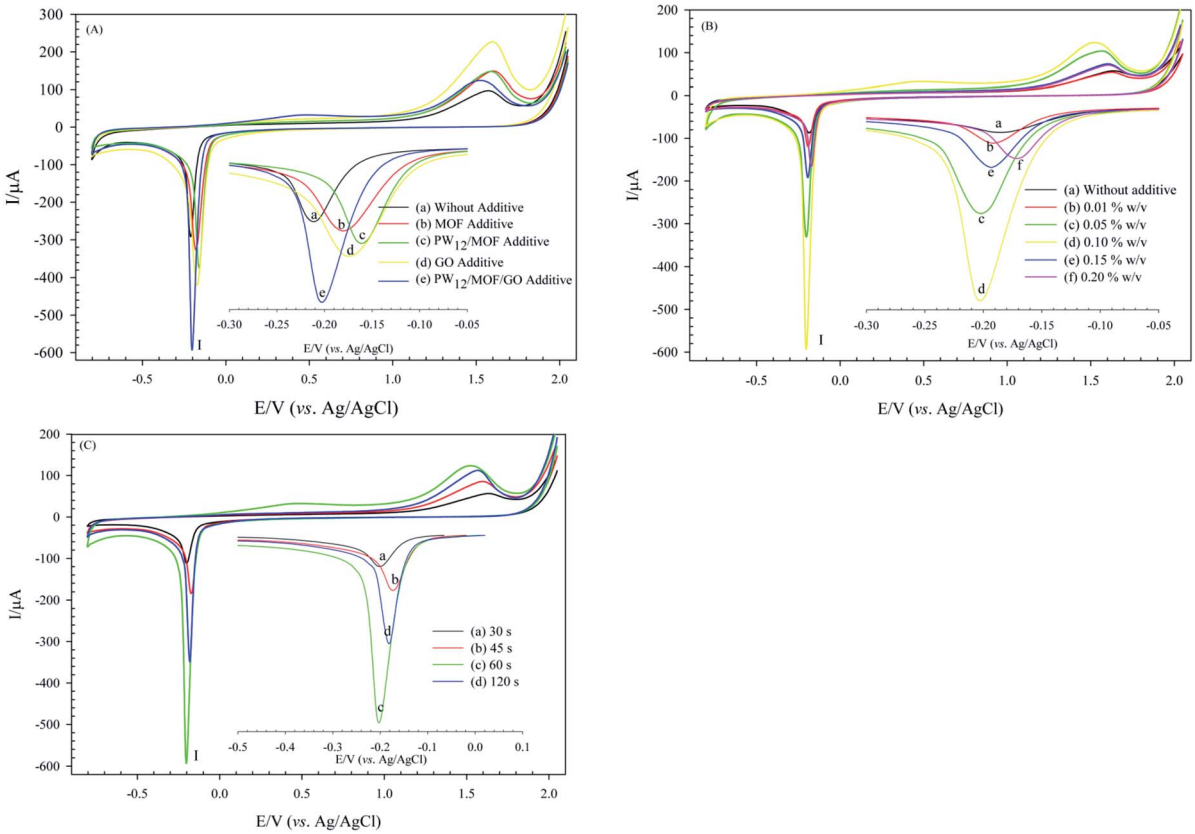

Fig. 7 Effect of (A) electrolyte additive type, (B) concentration of PW_{12}/MOF/GO additive; and (C) deposition time in 0.01 M H_3PO_4 at potential of −1.5 V; scan rate 50 mV s^{-1}, on the electrochemical activity of PW_{12}/MOF/P@ERGO/GCE.

modified electrode. The following experiments were performed using CV in H_3PO_4 (0.01 M) at the constant potential of −1.5 V, as shown in Fig. 7. The prepared modified electrode was signified as PW_{12}/MOF/P@ERGO/GCE through the text.

3.3.1. Effect of the electrolyte additive type. Fig. 7A, presents the effect of type of electrolyte additive (without additive, MOF, PW_{12}/MOF, GO, and PW_{12}/MOF/GO additive), on the electrochemical activity of the modified surface. The modified GCE, which is prepared in the presence of PW_{12}/MOF/GO additive (curve e), shows a more faradaic peak current (i_p, peak I) to other cases (curves a, b, c, and d). This phenomenon proves that PW_{12}/MOF/GO additive, due to the synergistic effects of these blocks, and its microstructure can improve the electrochemical activity of PW_{12}/MOF/P@ERGO/GCE.

3.3.2. Effect of electrolyte additive concentration. An optimum concentration of PW_{12}/MOF/GO additive was determined by electrochemical measurements in a wide range of additive concentrations (between 0.01 and 0.20% w/v) in 0.01 M H_3PO_4 aqueous solution. As displayed in Fig. 7B, the maximum peak I current of the modified electrode appeared in the presence of 0.10% w/v PW_{12}/MOF/GO additive (curve d). The current of peak I increased with PW_{12}/MOF/GO concentration up to 0.10% w/v and then decreased. This behavior depends on the viscosity of the additive. The viscosity is an essential parameter, which directly influences the ions diffusion. High viscosity leads to the aggregate of PW_{12}/MOF/GO and, causes its poor performance.

3.3.3. Effect of the electrodeposition time. The electrodeposition time is a crucial variable to be worth discussing. The effect electrodeposition time of 0.10% w/v PW_{12}/MOF/GO additive on the peak I current of PW_{12}/MOF/GO/GCE was performed from 30 s to 120 s at −1.5 V (*vs.* Ag/AgCl). To determine the optimum electrodeposition time, the CV curves of PW_{12}/MOF/P@ERGO in the presence of PW_{12}/MOF/GO additive (0.10% w/v) at different times were recorded. As shown in Fig. 7C, the modified GCE at 60 s have the most prominent peak I current than 30 s, 45 s, and 120 s, illustrating that it has a more electrochemical active area.

Therefore, prepared PW_{12}/MOF/GO/GCE in the presence of 0.10% w/v PW_{12}/MOF/GO additive at 60 s was set as modified GCE, and it chosen to continue the subsequent electrochemical tests. Such excellent performance of the modified GCE at 60 s can be for the following reason. With increasing deposition time up to 60 s, the thickness of the P@ERGO structure is raising, which leads to better electrochemical performance. However, a longer electrodeposition time of 120 s gave a PW_{12}/MOF/P@ERGO/GCE film with a thicker layer, which serves as a barrier layer and imparts resistance to the electron transfer.

3.4. Electrochemical studies of $[Fe(CN)_6]^{3-/4-}$ on the PW_{12}/MOF/P@ERGO/GCE

The electron transfer characteristics of the bare and the modified GCEs were appraised using voltammetric responses of

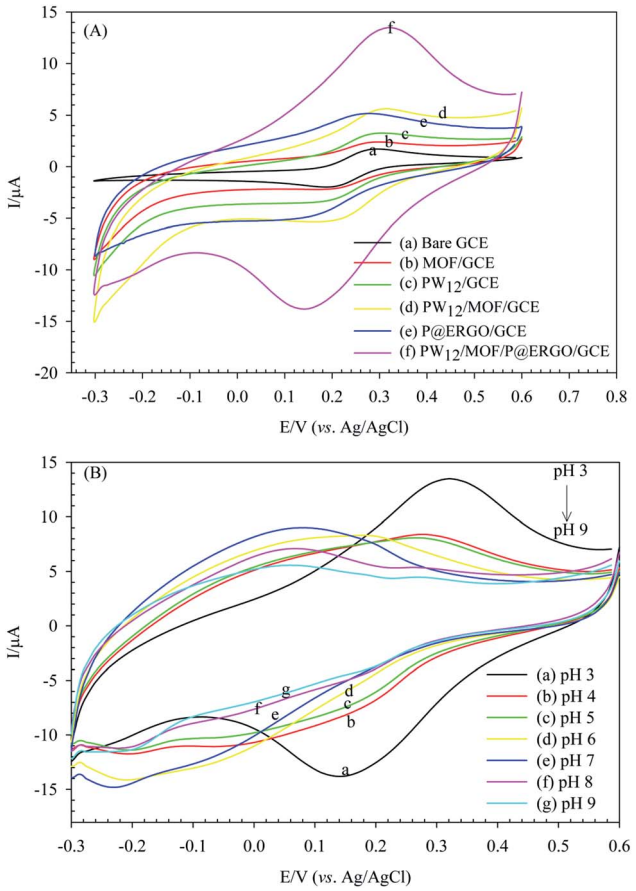

Fig. 8 CVs obtained in the presence of $[Fe(CN)_6]^{3-/4-}$ (0.5 mM) redox probe, in PBS solution (10.0 mM, pH 3) containing KCl (0.1 M) as supporting electrolyte, (A) on the bare GCE (a), MOF/GCE (b), PW_{12}/GCE (c), PW_{12}/MOF/GCE (d), P@ERGO/GCE (e), and PW_{12}/MOF/P@ERGO/GCE (f); Scan rate: 50 mV s^{-1}. (B) On the PW_{12}/MOF/P@ERGO/GCE in PBS solution (10.0 mM) at different pHs; scan rate: 50 mV s^{-1}.

$[Fe(CN)_6]^{3-/4-}$ redox probe. The thickness and electronic structure of the modifier affects the electron transfer kinetic of $[Fe(CN)_6]^{3-/4-}$ at the surface of the modified GCEs.[85] The bare GCE displays a redox couple separated by 92.9 mV with i_{pc} 1.68 μA in $[Fe(CN)_6]^{3-/4-}$ (0.5 mM) in PBS (10 mM, pH 3) containing KCl (0.1 M) (Fig. 8A, curve a). The immobilization of MOF, PW_{12}, and P@ERGO on the GCE leads to decrease in faradaic peak currents (i_p) (Fig. 8A, curve b, c, and e). These modifiers serve a kinetic barrier to charge transfer between $[Fe(CN)_6]^{3-/4-}$ and GCE surface, and decrease i_p. Moreover, PW_{12}/GCE, and P@ERGO/GCE also shows a significant increase in ΔE_p (Fig. 8A, curve c, e). The PW_{12}, and P@ERGO modifiers with negatively charges due to electrostatic repulsion with $[Fe(CN)_6]^{3-/4-}$ increase the ΔE_p. However, a lesser ΔE_p accompanied by an increasing of i_p was established for the PW_{12}/MOF/GCE, and PW_{12}/MOF/P@ERGO/GCE (Fig. 8A, curves d, f). It confirms that the synergistic effect of blocks can enhance the electron transfer kinetic at the GCE surface. The obtained quantitative information is given in Table 2.

Table 2 Electrochemical parameters extracted from CVs on the bare and modified GCEs in the presence of $[Fe(CN)_6]^{3-/4-}$ (0.5 mM) in PBS (10.0 mM, pH 3) containing KCl (0.1 M) as supporting electrolyte (Fig. 8A)

Electrode	ΔE/mV ± SD[a]	i_{pc}/μA ± SD[a]	i_{pa}/μA± SD[a]
Bare GCE	92.9 ± 1.2	1.68 ± 0.18	1.52 ± 0.13
MOF/GCE	80.0 ± 1.1	0.98 ± 0.06	0.99 ± 0.08
PW_{12}/GCE	107.0 ± 2.1	1.43 ± 0.17	1.73 ± 0.14
PW_{12}/MOF/GCE	80.0 ± 0.9	2.12 ± 0.15	2.47 ± 0.12
P@ERGO/GCE	115.8 ± 1.1	1.53 ± 0.19	1.55 ± 0.17
PW_{12}/MOF/P@ERGO/GCE	79.0 ± 1.2	2.12 ± 0.11	2.27 ± 0.12

[a] SD: standard deviation (from 3 data point).

Electrochemical studies showed that variation of the electrolyte pH effects on the electrochemical properties of PW_{12}/MOF/P@ERGO/GCE. Fig. 8B presents CVs of this modified electrode in $[Fe(CN)_6]^{3-/4-}$ (0.5 mM) at various pHs (pH 3 to pH 9). As shown, the ΔE_p increases and the i_ps decrease by increasing pH. However, almost no peak could be observed at pHs higher than 6. Indeed, with increasing pH, the concentration of OH^- increases. Therefore, the positively charged surface of the modified electrode is gradually neutralized. Thus, the electrostatic attraction between the surface of PW_{12}/MOF/P@ERGO/GCE and redox probe decreases and eventually disappears.

The electroactive surface area of the bare GCE, and PW_{12}/MOF/P@ERGO/GCE was estimated by CV measurements in $[Fe(CN)_6]^{3-/4-}$ (0.5 mM) containing KCl (0.1 M) at different scan rates (Fig. 9A and C, respectively). The electroactive surface area was calculated by using following Randles Sevcik equation (eqn (1)).[86]

$$i_p = 2.69 \times 10^5 n^{3/2} A D_0^{1/2} \nu^{1/2} C_{p1} \quad (1)$$

where i_p represents the anodic or cathodic peak current, n is the number of electrons transferred, A stands for the area of the electroactive surface (cm^2), D_0 denotes the diffusion co-efficient of $[Fe(CN)_6]^{3-/4-}$ (7.6×10^{-6} cm^2 s^{-1}), ν symbolize the scan rate (V s^{-1}), and C_p represents the concentration of the probe solution (M). The electroactive surface area of PW_{12}/MOF/P@ERGO/GCE is calculated to be 6.032 cm^2, according to the calibration equation of $i_p = 2.239\nu^{1/2} - 11.695$ ($R^2 = 0.974$) presented in Fig. 9D which is about 8.5 times larger than the bare electrode electroactive surface area (0.704 cm^2) with calibration equation of $i_p = 0.2615\nu^{1/2} + 0.218$ ($R^2 = 0.9974$) (Fig. 9B). Indeed, the high electroactive surface area of the PW_{12}/MOF/P@ERGO/GCE enhanced its electrochemical activity, which was shown in the previous parts.

3.5. Stability, repeatability, and reproducibility

Attaining a highly stable sensor is one of the main aims of analytical electrochemistry. The POM-based modified electrodes are usually stable in acidic aqueous solutions. The stability of the PW_{12}/MOF/P@ERGO/GCE was estimated by chronoamperometry (I-t) measurement at the fixed potential of

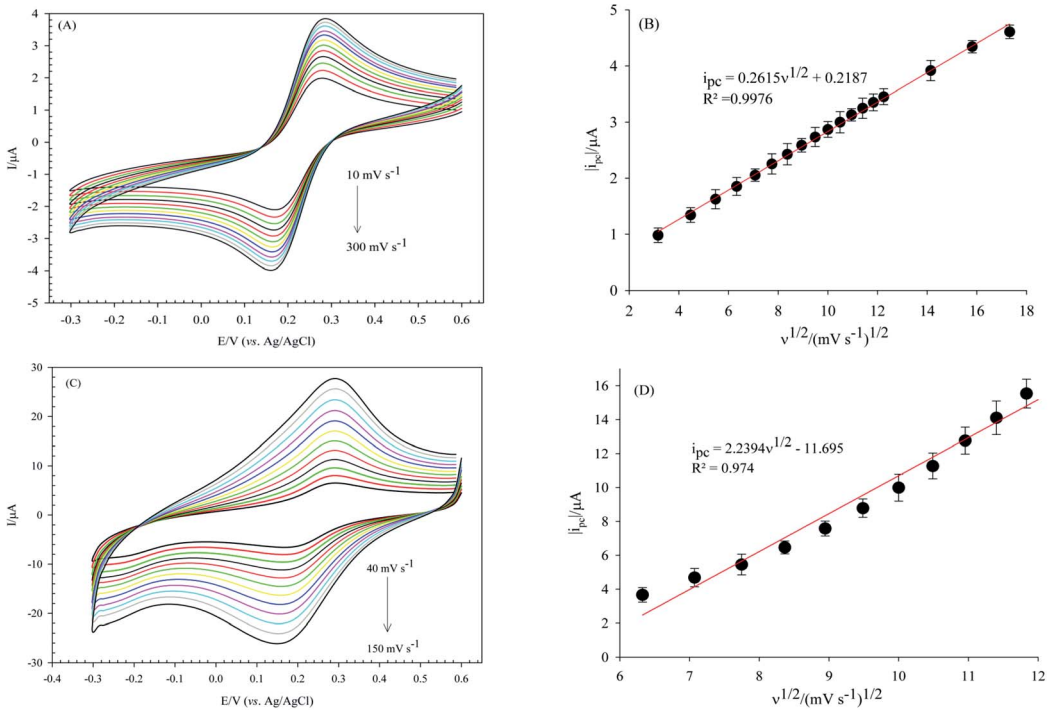

Fig. 9 CVs obtained in the presence of $[Fe(CN)_6]^{3-/4-}$ (0.5 mM) redox probe, in PBS solution (10.0 mM, pH 3) containing KCl (0.1 M) as supporting electrolyte, (A) on the bare GCE at different scan rates from 10 to 300 mV s^{-1}, (B) variations of the absolute value of cathodic peak currents on the bare GCE with square root of scan rates, (C) On the PW_{12}/MOF/P@ERGO/GCE at different scan rates from 40 to 150 mV s^{-1}, and (D) variations of the absolute value of cathodic peak currents on the PW_{12}/MOF/P@ERGO/GCE with square root of scan rates.

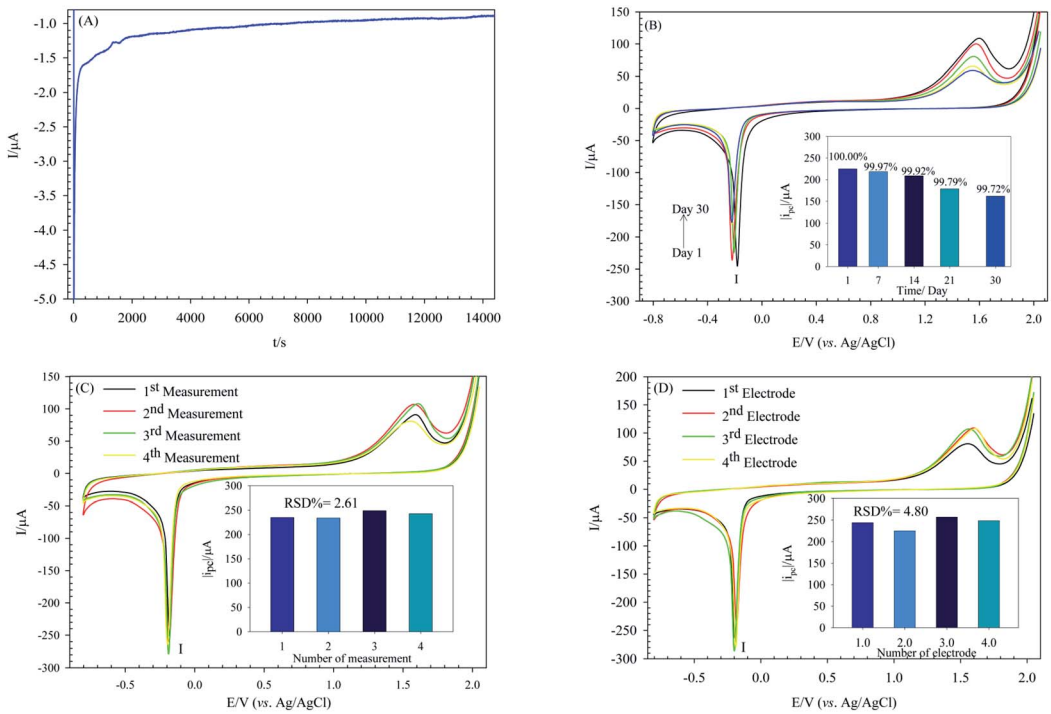

Fig. 10 (A) Stability investigation of PW_{12}/MOF/P@ERGO/GCE by chronoamperometry (I–t) measurement at the fixed potential of −0.175 V in 0.5 M H_2SO_4, (B) long-term stability of PW_{12}/MOF/P@ERGO/GCE in 0.5 M H_2SO_4 during a period of 30 days, (C) repeatability test of PW_{12}/MOF/P@ERGO/GCE in 0.5 M H_2SO_4, scan rate 50 mV s^{-1}, inset shows histogram of the peak I current of each measurement, and (D) reproducibility test of PW_{12}/MOF/P@ERGO/GCE in 0.5 M H_2SO_4, scan rate 50 mV s^{-1}, inset shows histogram of the peak I current of each modified GCE.

−0.175 V in 0.5 M H_2SO_4 solution. As seen in Fig. 10A, the performance of PW_{12}/MOF/P@ERGO/GCE is very stable up to 4 hours of measurement.

The long-term stability of the modified electrode was also investigated. For this purpose, peak I current of the PW_{12}/MOF/P@ERGO/GCE stored at ambient conditions over a month was recorded (Fig. 10B).

The results displayed that peak I current of the modified electrode remained at 99.97% of its primary current after 7 days, 99.92% after 14 days, 99.79% after 21 days, and 99.72% after a month.

The repeatability and reproducibility were also confirmed by repeatedly test. To certify the repeatability of PW_{12}/MOF/P@ERGO/GCE, four different CV tests were repeated with one modified GCE surface (Fig. 10C). The reproducibility was estimated using four same modified electrodes by CV (Fig. 10D). The results confirmed that the modified electrode has excellent repeatability and reproducibility with relative standard deviation (RSD) of 2.61% and 4.80%, respectively.

4. Conclusions

In summary, the preparation method of a novel modified GCE based on POM, MOF, and RGO hybrid nanocomposite (PW_{12}/MOF/P@ERGO/GCE) under the optimum conditions and its electrochemical properties has been investigated, comprehensively. The simplicity of preparation, high stability, good repeatability, and reproducibility are the features of the modified electrode. The modified GCE revealed a specific reduction peak that could be attributed to the HER processes. The PW_{12}/MOF/P@ERGO/GCE show a high electroactive surface area of 6.032 cm^2 resulting from the synergistic effect of PW_{12}, MOF, and P@ERGO, and the porous structure of the hybrid modifier. Furthermore, electrochemical measurements proved that different factors such as type and concentration of the electrolyte additive, and electrodeposition time affect the electrochemical activity of the modified GCE.

Conflicts of interest

There are no conflicts to declare.

Acknowledgements

The authors gratefully acknowledge the financial support of this work by the Research Council of the University of Hormozgan.

References

1 L. Wang, T. Meng, J. Sun, S. Wu, M. Zhang, H. Wang and Y. Zhang, *Anal. Chim. Acta*, 2019, **1047**, 28–35.
2 J. Sun, S. Abednatanzi, P. Van Der Voort, Y.-Y. Liu and K. Leus, *Catalysts*, 2020, **10**, 578.
3 M. Samaniyan, M. Mirzaei, R. Khajavian, H. Eshtiagh-Hosseini and C. Streb, *ACS Catal.*, 2019, **9**, 10174–10191.
4 E. Rtibi, M. Abderrabba, S. Ayadi and B. Champagne, *Inorg. Chem.*, 2019, **58**, 11210–11219.
5 J. M. Clemente-Juan, E. Coronado and A. Gaita-Ariño, *Chem. Soc. Rev.*, 2012, **41**, 7464–7478.
6 S. Dianat, A.-K. Bordbar, S. Tangestaninejad, B. Yadollahi, R. Amiri, S.-H. Zarkesh-Esfahani and P. Habibi, *J. Inorg. Biochem.*, 2015, **152**, 74–81.
7 S. Dianat, A. Bordbar, S. Tangestaninejad, S. Zarkesh-Esfahani, P. Habibi and A. A. Kajani, *J. Iran. Chem. Soc.*, 2016, **13**, 1895–1904.
8 A. X. Yan, S. Yao, Y. G. Li, Z. M. Zhang, Y. Lu, W. L. Chen and E. B. Wang, *Chem.–Eur. J.*, 2014, **20**, 6927–6933.
9 A. Karimi-Takallo, S. Dianat and A. Hatefi-Mehrjardi, *J. Electroanal. Chem.*, 2021, **886**, 115139.
10 M. Sharifi, S. Dianat and A. Hosseinian, *RSC Adv.*, 2021, **11**, 8993–9007.
11 F. Boussema, R. Haddad, Y. Ghandour, M. S. Belkhiria, M. Holzinger, A. Maaref and S. Cosnier, *Electrochim. Acta*, 2016, **222**, 402–408.
12 Q. Wang, J. Khungwa, L. Li, Y. Liu, X. Wang and S. Wang, *J. Electroanal. Chem.*, 2018, **824**, 91–98.
13 M. Green, J. Harries, G. Wakefield and R. Taylor, *J. Am. Chem. Soc.*, 2005, **127**, 12812–12813.
14 R. Liu, Y. Zhang, J. Ding, R. Wang and M. Yu, *Sep. Purif. Technol.*, 2017, **174**, 84–88.
15 S. Maity, B. Neethu, T. Kella, D. Shee, P. P. Das and S. S. Mal, *J. Energy Storage*, 2021, **40**, 102727.
16 J. Selvam, B. Samannan, P. Peter and J. Thavasikani, *Polym. Polym. Compos.*, 2021, **29**, 373–382.
17 C. T. Buru and O. K. Farha, *ACS Appl. Mater. Interfaces*, 2020, **12**, 5345–5360.
18 P. Mialane, C. Mellot-Draznieks, P. Gairola, M. Duguet, Y. Benseghir, O. Oms and A. Dolbecq, *Chem. Soc. Rev.*, 2021, **50**, 6152–6220.
19 M. Bonneau, C. Lavenn, P. Ginet, K.-i. Otake and S. Kitagawa, *Green Chem.*, 2020, **22**, 718–724.
20 K. Shen, X. Chen, J. Chen and Y. Li, *ACS Catal.*, 2016, **6**, 5887–5903.
21 H. T. Nguyen, D. N. Doan and T. Truong, *J. Mol. Catal. A: Chem.*, 2017, **426**, 141–149.
22 Q. Wang and D. Astruc, *Chem. Rev.*, 2019, **120**, 1438–1511.
23 K. N. Chappanda, O. Shekhah, O. Yassine, S. P. Patole, M. Eddaoudi and K. N. Salama, *Sens. Actuators, B*, 2018, **257**, 609–619.
24 L. Wang, Z. Hu, S. Wu, J. Pan, X. Xu and X. Niu, *Anal. Chim. Acta*, 2020, **1121**, 26–34.
25 M. X. Wu and Y. W. Yang, *Adv. Mater.*, 2017, **29**, 1606134.
26 J. Cao, X. Li and H. Tian, *Curr. Med. Chem.*, 2020, **27**, 5949–5969.
27 Y. Y. Cai, Q. Yang, Z. Y. Zhu, Q. H. Sun, A. M. Zhu, Q. G. Zhang and Q. L. Liu, *J. Membr. Sci.*, 2019, **590**, 117277.
28 Z.-Q. Shi, N.-N. Ji, M.-H. Wang and G. Li, *Inorg. Chem.*, 2020, **59**, 4781–4789.
29 E. D. Spoerke, L. J. Small, M. E. Foster, J. Wheeler, A. M. Ullman, V. Stavila, M. Rodriguez and M. D. Allendorf, *J. Phys. Chem. C*, 2017, **121**, 4816–4824.
30 J. Dou, C. Zhu, H. Wang, Y. Han, S. Ma, X. Niu, N. Li, C. Shi, Z. Qiu and H. Zhou, *Adv. Mater.*, 2021, 2102947.

31 S. Gao, Y. Sui, F. Wei, J. Qi, Q. Meng and Y. He, *J. Mater. Sci.*, 2018, **53**, 6807–6818.
32 Y. Wang, Y. Liu, H. Wang, W. Liu, Y. Li, J. Zhang, H. Hou and J. Yang, *ACS Appl. Energy Mater.*, 2019, **2**, 2063–2071.
33 D. Wang, D. Jana and Y. Zhao, *Acc. Chem. Res.*, 2020, **53**, 1389–1400.
34 A. Bieniek, A. P. Terzyk, M. Wiśniewski, K. Roszek, P. Kowalczyk, L. Sarkisov, S. Keskin and K. Kaneko, *Prog. Mater. Sci.*, 2021, **117**, 100743.
35 Y. Han, H. Xu, Y. Su, Z.-l. Xu, K. Wang and W. Wang, *J. Catal.*, 2019, **370**, 70–78.
36 Y. Li, Y. Xu, W. Yang, W. Shen, H. Xue and H. Pang, *Small*, 2018, **14**, 1704435.
37 S. Wu, J. Liu, H. Wang and H. Yan, *Int. J. Energy Res.*, 2019, **43**, 697–716.
38 X. Lian, Y. Huang, Y. Zhu, Y. Fang, R. Zhao, E. Joseph, J. Li, J. P. Pellois and H. C. Zhou, *Angew. Chem.*, 2018, **130**, 5827–5832.
39 S. S. Nadar, L. Vaidya and V. K. Rathod, *Int. J. Biol. Macromol.*, 2020, **149**, 861–876.
40 C. Freire, D. M. Fernandes, M. Nunes and V. K. Abdelkader, *ChemCatChem*, 2018, **10**, 1703–1730.
41 D. Shi, R. Zheng, C.-S. Liu, D.-M. Chen, J. Zhao and M. Du, *Inorg. Chem.*, 2019, **58**, 7229–7235.
42 G. Férey, C. Mellot-Draznieks, C. Serre, F. Millange, J. Dutour, S. Surblé and I. Margiolaki, *Science*, 2005, **309**, 2040–2042.
43 W. Salomon, F.-J. Yazigi, C. Roch-Marchal, P. Mialane, P. Horcajada, C. Serre, M. Haouas, F. Taulelle and A. Dolbecq, *Dalton Trans.*, 2014, **43**, 12698–12705.
44 H. Wan, C. Chen, Z. Wu, Y. Que, Y. Feng, W. Wang, L. Wang, G. Guan and X. Liu, *ChemCatChem*, 2015, **7**, 441–449.
45 Q. Y. Li, L. Zhang, Y. X. Xu, Q. Li, H. Xue and H. Pang, *ACS Sustainable Chem. Eng.*, 2019, **7**, 5027–5033.
46 L. E. Lange and S. K. Obendorf, *ACS Appl. Mater. Interfaces*, 2015, **7**, 3974–3980.
47 Y. Dong, J. Zhang, Y. Yang, L. Qiu, D. Xia, K. Lin, J. Wang, X. Fan and R. Fan, *Angew. Chem., Int. Ed.*, 2019, **58**, 17610–17615.
48 M. Wei, X. Wang and X. Duan, *Chem.–Eur. J.*, 2013, **19**, 1607–1616.
49 H. Yang, J. Li, H. Zhang, Y. Lv and S. Gao, *Microporous Mesoporous Mater.*, 2014, **195**, 87–91.
50 S. Li, L. Zhang, K. P. O'Halloran, H. Ma and H. Pang, *Dalton Trans.*, 2015, **44**, 2062–2065.
51 G. Paille, M. Gomez-Mingot, C. Roch-Marchal, M. Haouas, Y. Benseghir, T. Pino, M.-H. Ha-Thi, G. Landrot, P. Mialane and M. Fontecave, *ACS Appl. Mater. Interfaces*, 2019, **11**, 47837–47845.
52 K. S. Novoselov, A. K. Geim, S. V. Morozov, D.-e. Jiang, Y. Zhang, S. V. Dubonos, I. V. Grigorieva and A. A. Firsov, *Science*, 2004, **306**, 666–669.
53 V. Dhinakaran, M. Lavanya, K. Vigneswari, M. Ravichandran and M. Vijayakumar, *Mater. Today: Proc.*, 2020, **27**, 824–828.
54 A. K. Geim, *science*, 2009, **324**, 1530–1534.
55 Y. Kim and S. Shanmugam, *ACS Appl. Mater. Interfaces*, 2013, **5**, 12197–12204.
56 N. Mizuno and M. Misono, *Chem. Rev.*, 1998, **98**, 199–218.
57 D. M. Fernandes, M. P. Araujo, A. Haider, A. S. Mougharbel, A. J. Fernandes, U. Kortz and C. Freire, *ChemElectroChem*, 2018, **5**, 273–283.
58 J. Qin, F. Zhou, H. Xiao, R. Ren and Z.-S. Wu, *Sci. China Mater.*, 2018, **61**, 233–242.
59 H. Asadollahi-yazdi, M. Shariati, A. Imam and M. Ghatee, *J. Compos. Mater.*, 2017, **51**, 3053–3064.
60 B. Suma, P. S. Adarakatti, S. K. Kempahanumakkagari and P. Malingappa, *Mater. Chem. Phys.*, 2019, **229**, 269–278.
61 S.-K. Hwang, S. J. Patil, N. R. Chodankar, Y. S. Huh and Y.-K. Han, *Chem. Eng. J.*, 2022, **427**, 131854.
62 H. Li, S. Pang, S. Wu, X. Feng, K. Müllen and C. Bubeck, *J. Am. Chem. Soc.*, 2011, **133**, 9423–9429.
63 J. Chen, S. Liu, W. Feng, G. Zhang and F. Yang, *Phys. Chem. Chem. Phys.*, 2013, **15**, 5664–5669.
64 D. Zhou and B. H. Han, *Adv. Funct. Mater.*, 2010, **20**, 2717–2722.
65 W. Guo, X. Tong and S. Liu, *Electrochim. Acta*, 2015, **173**, 540–550.
66 L. Chen, Y. Tang, K. Wang, C. Liu and S. Luo, *Electrochem. Commun.*, 2011, **13**, 133–137.
67 Y. Mai, M. Zhou, H. Ling, F. Chen, W. Lian and X. Jie, *Appl. Surf. Sci.*, 2018, **433**, 232–239.
68 M. Mirzaee, C. Dehghanian and K. S. Bokati, *J. Electroanal. Chem.*, 2018, **813**, 152–162.
69 T. Wei, M. Zhang, P. Wu, Y.-J. Tang, S.-L. Li, F.-C. Shen, X.-L. Wang, X.-P. Zhou and Y.-Q. Lan, *Nano Energy*, 2017, **34**, 205–214.
70 W. Zhang, G. Jia, Z. Li, C. Yuan, Y. Bai and D. Fu, *Adv. Mater. Interfaces*, 2017, **4**, 1601241.
71 K. Gopalakrishnan, S. Sultan, A. Govindaraj and C. Rao, *Nano Energy*, 2015, **12**, 52–58.
72 D. Zhang, Y. Zhang, Y. Luo, Y. Zhang, X. Li, X. Yu, H. Ding, P. K. Chu and L. Sun, *Nano Res.*, 2018, **11**, 1651–1663.
73 R. Ding, J. Zhang, J. Qi, Z. Li, C. Wang and M. Chen, *ACS Appl. Mater. Interfaces*, 2018, **10**, 13470–13478.
74 K. Bindumadhavan, P.-Y. Chang and R.-a. Doong, *Electrochim. Acta*, 2017, **243**, 282–290.
75 S. Bag, B. Mondal, A. K. Das and C. R. Raj, *Electrochim. Acta*, 2015, **163**, 16–23.
76 Z.-J. Lu, S.-J. Bao, Y.-T. Gou, C.-J. Cai, C.-C. Ji, M.-W. Xu, J. Song and R. Wang, *RSC Adv.*, 2013, **3**, 3990–3995.
77 Z. Wang, P. Li, Y. Chen, J. He, J. Liu, W. Zhang and Y. Li, *J. Power Sources*, 2014, **263**, 246–251.
78 L.-s. Cui, X.-m. Meng, Y.-g. Li, K.-r. Huang, Y.-c. Li, J.-q. Long and P.-f. Yao, *CrystEngComm*, 2019, **21**, 3798–3809.
79 M. Barsukova, D. Samsonenko, T. Goncharova, A. Potapov, S. Sapchenko, D. Dybtsev and V. Fedin, *Russ. Chem. Bull.*, 2016, **65**, 2914–2919.
80 D. C. Marcano, D. V. Kosynkin, J. M. Berlin, A. Sinitskii, Z. Sun, A. Slesarev, L. B. Alemany, W. Lu and J. M. Tour, *ACS Nano*, 2010, **4**, 4806–4814.
81 S. Bykkam, K. Rao, C. Chakra and T. Thunugunta, *Int. J. Adv. Biotechnol. Res.*, 2013, **4**, 142–146.
82 N. Raghavan, S. Thangavel and G. Venugopal, *Mater. Sci. Semicond. Process.*, 2015, **30**, 321–329.

83 D. Jana, H. K. Kolli, S. Sabnam and S. K. Das, *Chem. Commun.*, 2021, **57**, 9910–9913.
84 R. Hashemniaye-Torshizi, N. Ashraf, M. H. Arbab-Zavar and S. Dianat, *Catal. Sci. Technol.*, 2021, **11**, 1098–1109.
85 S. Dianat, A. Hatefi-Mehrjardi and K. Mahmoodzadeh, *New J. Chem.*, 2019, **43**, 1388–1397.
86 D. Zhu, H. Ma, Q. Zhen, J. Xin, L. Tan, C. Zhang, X. Wang and B. Xiao, *Appl. Surf. Sci.*, 2020, **526**, 146721.